

Benthic effects on the polarization of light in shallow waters

Alexander A. Gilerson,^{1,*} Jan Stepinski,¹ Amir I. Ibrahim,¹ Yu You,^{2,3}
James M. Sullivan,^{4,5} Michael S. Twardowski,⁴ Heidi M. Dierssen,⁶
Brandon Russell,⁶ Molly E. Cummings,⁷ Parrish Brady,⁷
Samir A. Ahmed,¹ and George W. Kattawar²

¹Optical Remote Sensing Laboratory, the City College of the City University of New York, New York, New York 10031, USA

²Department of Physics and Astronomy, Texas A&M University, College Station, Texas 77843-4242, USA

³Schlumberger/WesternGeco, 3750 Briarpark, Houston 77042, USA

⁴WET Labs Inc., 70 Dean Knauss Road, Narragansett, Rhode Island 02882-1197, USA

⁵University of Rhode Island, Graduate School of Oceanography, South Ferry Road, Narragansett, Rhode Island 02882-1197, USA

⁶Department of Marine Sciences, University of Connecticut Avery Point, 1080 Shennecossett Road, Groton, Connecticut 06340-6048, USA

⁷Section of Integrative Biology, University of Texas, Austin, Texas 78712, USA

*Corresponding author: gilerson@ccny.cuny.edu

Received 31 July 2013; revised 7 November 2013; accepted 16 November 2013;
posted 18 November 2013 (Doc. ID 194876); published 13 December 2013

Measurements of the upwelling polarized radiance in relatively shallow waters of varying depths and benthic conditions are compared to simulations, revealing the depolarizing nature of the seafloor. The simulations, executed with the software package RayXP, are solutions to the vector radiative transfer equation, which depends on the incident light field and three types of parameters: inherent optical properties, the scattering matrix, and the benthic reflectance. These were measured directly or calculated from measurements with additional assumptions. Specifically, the Lambertian model used to simulate benthic reflectances is something of a simplification of reality, but the bottoms used in this study are found to be crucial for accurate simulations of polarization. Comparisons of simulations with and without bottom contributions show that only the former corroborate measurements of the Stokes components and the degree of linear polarization (DoLP) collected by the polarimeter developed at the City College of New York. Because this polarimeter is multiangular and hyperspectral, errors can be computed pointwise over a large range of scattering angles and wavelengths. Trends also become apparent. DoLP is highly sensitive to the benthic reflectance and to the incident wavelength, peaking in the red band, but the angle of linear polarization is almost spectrally constant and independent of the bottom. These results can thus facilitate the detection of benthic materials as well as future studies of camouflage by benthic biota; to hide underwater successfully, animals must reflect light just as depolarized as that reflected by benthic materials. © 2013 Optical Society of America

OCIS codes: (010.4450) Oceanic optics; (010.4458) Oceanic scattering; (010.5620) Radiative transfer; (290.5855) Scattering, polarization; (300.6550) Spectroscopy, visible.

<http://dx.doi.org/10.1364/AO.52.008685>

1. Introduction

Direct measurements and numerical simulations have been used to study polarization in the ocean since the middle of the twentieth century [1–3]. Most

of the measurements were collected in open-water, pelagic habitats. Coastal and benthic environments also have been studied [4–7], but the impact of the bottom was not specifically analyzed. This deficiency in information about the polarization properties of the shallow ocean impedes engineering applications, such as remote sensing and target detection, and hinders our understanding of the camouflage and communication techniques of marine animals. While polarization in the open ocean is largely determined by the water column and the atmosphere, in shallow waters light reflected from the bottom significantly contributes to the intensity, and thereby polarization, measured near the surface. Furthermore, because the bottom is not a plane of rock but rather an irregularly spaced, varicolored, heterogeneous surface, its albedo is highly variable and difficult to measure directly.

Several studies have previously focused on the hyperspectral effects of optically shallow bottoms on above-water and underwater upwelling radiance [8–11]. But except for Zhang *et al.* [12], who measured the polarization properties of packed benthic sediments, none of them have considered the polarization of light. This study reports some of the first comprehensive results of concurrent hyperspectral measurements of the polarized light fields in shallow waters compared with simulations using vector radiative transfer (RT) code.

All experimental datasets were collected in stations around the coast of the Florida Keys in Greater Florida Bay. Although the water clarity and the seafloor in the area of the chosen sites in the Florida Keys have been studied previously [13,14], accurate measurements of the inherent optical properties (IOPs) and benthic reflectance are crucial for validating concurrent measurements of polarization. The measurement techniques are described in detail in Section 2. Their validation is performed by entering the aforementioned properties of both water and seafloor into the vector radiation transfer model described in Section 3. Comparisons between measurements and the complete numerical model begin in Section 4 with the deepest of the stations. The IOPs, bottom reflectance, radiance field, polarization, and numerical error are addressed, each in its own subsection. The same sequence of subsections is then used in Section 5 to present the remaining three shallower stations. All stations are summarized for several wavelengths and viewing geometries in Section 6. Section 7 concludes with a discussion of the implications for remote sensing as well as biology.

2. Field Experiment

All measurements were taken from a research vessel in the Florida Keys in January 2011 in shallow (approximately 2–5 m) and relatively deep (approximately 18 m) waters. Each depth was obtained from the on-board sounder. The seafloor at each station consisted of varying proportions of sand, different types of sea grass, and coral. Its benthic reflectance

was measured using a diver-operated spectrometer (Night Sea LLC) [15].

Characterized by their reflectance spectra, the seafloors actually constitute the final “layer” of the RT model, which is elaborated on in Section 3. The remaining layers, or more accurately layer types, are moving upward from the bottom, the oceanic layer (water molecules [16] + hydrosols), the air–water interface, and the atmospheric layer (air molecules [17,18] + aerosol). The properties of the hydrosol were measured and subsequently used to replicate coincident measurements of the polarized light field with the RT model.

Absorption (a) and attenuation (c) coefficients were measured hyperspectrally in the visible spectrum using an ac-s instrument (WET Labs). The volume scattering function (VSF) was measured with the multiangle scattering optical tool (MASCOT), designed to sample monochromatic light of 658 nm at 20 Hz over a range of scattering angles from 10° to 170°. The MASCOT source beam is a 30 mW laser diode expanded with a Galilean 2× beam expander, and it is transmitted through a wedge depolarizer to provide the unpolarized light required to measure the VSF [19–21]. Polarization elements of the VSF were measured by placing various polarizers over the monochromatic light source. These measurements can resolve the top row of the Mueller scattering matrix, described in Section 3, and thereby complement the numerical model with empirical data.

The polarized light field in the water column was measured with the multiangular hyperspectral polarimeter, developed at the City College of New York (CCNY) [22]. This instrument can measure the polarized light field at 136 wavelengths ranging from blue (400 nm) to near infrared (801 nm). Its three hyperspectral radiance sensors (HyperOCRs, Satlantic) each receive light through a linear polarizer (Edmund Optics) set to a specific angle: 0°, 45°, and 90° with respect to a reference axis. At this point, one should be careful not to confuse the angles used in describing the geometry of the polarimeter. While the angles of the linear polarizers are held fixed, the polarimeter itself can be rotated in a full circle of viewing angles. To distinguish these angles from the conventional viewing and viewing azimuth angles, they are henceforth referred to as *instrument* angles. Figure 1 explains the distinction. The polarimeter is mounted on a scanning system controlled by an underwater electric stepper motor (Newmark Systems, Inc.). Additional details about this instrument are available in [23].

Although this study is primarily focused on polarization, it also performs preliminary validation with a conventional estimate of reflectance, specifically the upwelling radiance at a 1 m depth normalized by the downwelling irradiance in air. The properties of air—the topmost layer of the RT model—were not measured *in situ* but rather taken from the moderate resolution imaging spectroradiometer (MODIS) for use in simulations. The downwelling irradiance,

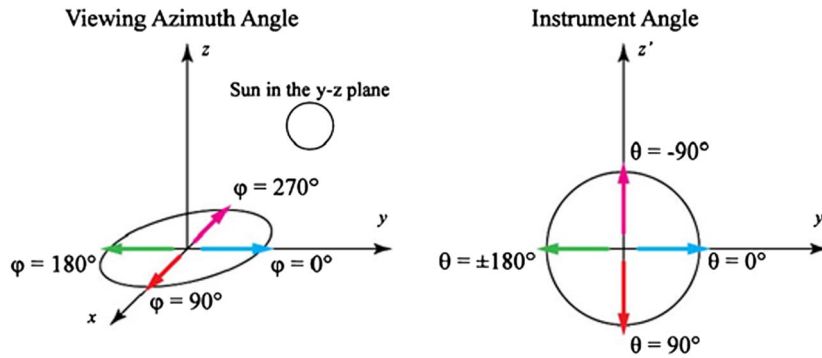


Fig. 1. Definition of the viewing azimuth angle and the polarimeter's instrument angle.

however, was measured by an irradiance sensor (HyperOCR, Satlantic) mounted in an unobstructed and elevated position on the research vessel.

3. Numerical Model

Field measurements are compared with numerical simulations with and without bottoms to reveal how the bottom affects the bidirectional transmission of light through water. The software RayXP [24,25] is used to facilitate such simulations. An assumption inherent in the program is that any media through which radiation propagates consists of homogeneously scattering plane-parallel layers. The three general layers have already been introduced in Section 2: the atmosphere, the water column, and the seafloor. An additional air-water interface is also required; it is essentially a plane punctuated by isotropic waves.

The layers, air and ocean, through which light is transmitted are actually divided into multiple and also plane-parallel sublayers. Each of these sublayers is characterized by its own molecular and aerosol or hydrosol extinction coefficient (c), single scattering albedo (ω), and 4×4 scattering (Mueller) matrix. There are just two sublayers for the air: the atmosphere and the oceanic spray. The water column is divided according to measurements; that is, if the IOPs of a 5 m station are measured every 0.2 m, then the model would contain 25 layers, each representing a 0.2 m transverse slice of the ocean. Molecular component was included in all of these layers [16,26]. But only one scattering matrix was measured for the whole water column; it is therefore the same for every sublayer.

The scattering matrix is defined as

$$\mathbf{F} = \begin{bmatrix} F_{11} & F_{12} & 0 & 0 \\ F_{12} & F_{22} & 0 & 0 \\ 0 & 0 & F_{33} & 0 \\ 0 & 0 & 0 & F_{44} \end{bmatrix}.$$

Along with the IOPs, it can be used to express the propagation of light through the medium with the vector RT equation (VRTE):

$$\mu \frac{\partial \mathbf{S}(\tau, \mathbf{n})}{\partial \tau} = \frac{\omega(\tau)}{4\pi} \iint \mathbf{F}(\tau, \mathbf{n}, \mathbf{n}') \mathbf{S}(\tau, \mathbf{n}') d\mathbf{n}' - \mathbf{S}(\tau, \mathbf{n}), \quad (1)$$

where τ is the optical thickness of the medium. This integrodifferential equation is to be solved for the Stokes vector $\mathbf{S}(\tau, \mathbf{n}) = [I(\tau, \mathbf{n}) \mathbf{Q}(\tau, \mathbf{n}) U(\tau, \mathbf{n}) V(\tau, \mathbf{n})]^T$, whose components represent the state of polarization in the direction normal to the surface given by $\mathbf{n}(\mu, \varphi)$, where $\mu = \cos \gamma$, and γ and φ are the zenith and azimuth angles in a spherical coordinate system. The I component represents total radiance, Q represents the horizontal and vertical states of polarization, U the $\pm 45^\circ$ states, and V the circular states. In the measurements and simulations conducted in this study, circular polarization is assumed to be negligible [23]. The other components are solved for using the RayXP algorithm, which incorporates various techniques, collectively known as the multi-component approach, to minimize computational time. The MCA separates the peaked component of the phase matrix of the scatterer from the other, more diffuse component. Further segmentation of each of these two components then facilitates solutions that are accurate relative to the general RT solutions while being much more computationally efficient [24,25].

From the Stokes components, the degree of linear polarization (DoLP) can be computed as reported in You *et al.* [19]:

$$\text{DoLP} = \frac{\sqrt{Q^2 + U^2}}{I}. \quad (2)$$

The orientation of the light wave is described by the angle of linear polarization (AoLP), which can also be computed from the Stokes components:

$$\text{AoLP} = \frac{1}{2} \tan^{-1} \left(\frac{U}{Q} \right). \quad (3)$$

The AoLP can vary from -90° to 90° [27]. At these endpoints, light propagates perpendicular to the reference plane, defined to be the meridian plane in this study, and when $\text{AoLP} = 0^\circ$, the wave is said to be in the reference plane.

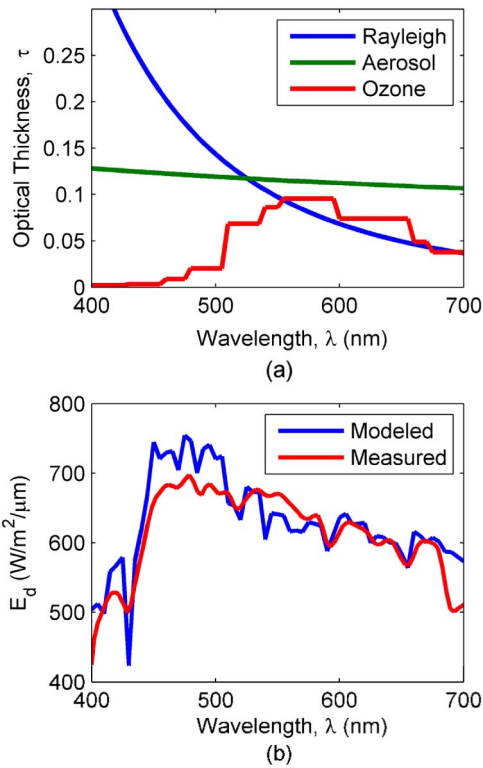


Fig. 2. Modeling the passage of light through the atmospheric layer. (a) Decomposes the optical thickness τ of the atmosphere into its components, as measured by MODIS. The resulting downwelling irradiance E_d from Eq. (4) is compared to the measured values in (b).

A. Atmospheric Layer: Aerosols

Measurements of downwelling irradiance E_d in air cannot be entered into RayXP directly to specify the source of light propagating through water. Since the program restricts user inputs to optical properties, the level 2 aerosol optical thickness product collected by MODIS on its pass over the Florida Keys on a specific day is combined with a default scattering matrix for oceanic aerosols in simulations of the stations investigated on that day. A typical spectrum of the optical thickness is shown in Fig. 2(a). RayXP does not allow E_d to be directly inputted by the user, but the value it uses can be approximated as [28]

$$E_d(\lambda) = \exp\left(-\frac{0.5\tau_r(\lambda) + 0.14\tau_a(\lambda) + \tau_{oz}(\lambda)}{\cos\theta_s}\right)E_0(\lambda)\cos\theta_s, \quad (4)$$

where τ_r , τ_a , and τ_{oz} are the Rayleigh, aerosol, and ozone optical thicknesses, all obtained from MODIS; E_0 is the extraterrestrial irradiance; and θ_s is the sun zenith angle, specified for each station in Table 1. Simulations of the radiance field in the water column can then be normalized by the simulated E_d just as measurements of the radiance field can be normalized by the measurements of E_d . The normalization by irradiance should not have much of an effect beyond simplifying units; Fig. 2(b) confirms a strong correlation between the numerical model and the measurements.

B. Oceanic Layer: Scattering Matrix

Unlike the optical properties of the atmosphere, the water IOPs that specify the VRTE have been measured *in situ*. But whereas raw measurements of the optical thicknesses of particulates and molecules can be passed directly to RayXP, those of the scattering matrix, F in Eq. (1), cannot. There are two reasons. First, the scattering angles used by the MASCOT do not adequately coincide with those used by RayXP. Second, the MASCOT does not measure the diagonal components of the scattering matrix. This section explains how these two obstacles can be overcome with numerical methods and analytical models.

The MASCOT is limited to measuring the volume scattering function $\beta(\psi)$ only at scattering angles ψ ranging from 10° to 170° at 10° increments. The full hemisphere at a finer angular resolution is required for RayXP. However, F_{11} and F_{12} can be extrapolated from the unpolarized and polarized measurements, respectively, for use in the simulations. A crucial, overarching assumption is that the scattering matrix is wavelength-independent; measurements from MASCOT at 658 nm are ultimately used in RayXP for simulations at any wavelength between 400 and 700 nm. Scattering by water molecules changes significantly over this domain, but this dependence is inherent in RayXP. Indeed, the results will show that polarization is sensitive to scattering and absorption by water. So the objective of the MASCOT must be to isolate scattering by larger molecules and particles, and since the contribution of water to total scattering is lowest in red light, 658 nm is an appropriate wavelength at which to collect measurements.

The phase function is related to the volume scattering function by

Table 1. Characteristic Parameters of the Four Stations

Station	Depth (m)	Type of Bottom	Phase Matrix Parameters		Sun Elevation Angle ($^\circ$)
			g	ρ	
40	18.0	Sandy with some coral	0.89	0.17	42.0
49	5.0	Sandy with some sea grass	0.88	0.18	28.0
36	1.5	Sea grass	0.83	0.18	20.5
30	4.5	Coral	0.85	0.20	20.0

$$F_{11}(\psi) = \frac{\beta(\psi)}{b_{658}}, \quad (5)$$

where b_{658} is the total scattering coefficient. Analytically, $b_{658} = 2\pi \int_0^\pi \sin(\psi)\beta(\psi)d\psi$, so multiplying both sides of Eq. (5) by the sine term and integrating over all scattering angles suggests that $2\pi \int_0^\pi \sin(\psi)F_{11}(\psi)d\psi = 1$. The unity of the integral of the phase function is crucial for accurate simulations, but this requirement is not immediately satisfied in the measurements. The transmission tube of the ac-9 (WET Labs, similar to ac-s except measurements are at nine wavelengths) is limited to acceptance angles between 0.93° and 180° , not from 0 to 180° , thus partially compromising the accuracy of scattering measurements. Because forward scattering, which occurs at small scattering angles, predominates in the water, this small difference of 0.93° can cause measurements of b_{658} to differ by up to 30% from the true values. Extrapolation of the phase function into the forward scattering region must account for this error.

Begin with the measurements of the VSF, which are available from 10° to 170° . The goal is the phase function extended to all scattering angles; let it be called $F_{11,\text{ext}}$. The segments from 0° to 10° and 170° to 180° , the endpoints being inclusive, will be the Henyey–Greenstein (H-G) phase function, $F_{11,\text{HG}}$. This analytic formulation of the phase function is characterized by the anisotropy factor g , which is readily computed by fitting the measurements with the equation for $F_{11,\text{HG}}$. In order to gauge the error in the measurements as well as the fit, an extended VSF β_{ext} can then be constructed and its integral compared to b_{658} . To avoid using b_{658} in creating the extension that will be compared to b_{658} , a ratio of the 10° endpoints of the measurements and the H-G function is used for the forward scattering direction. Since backscattering is minimal, the VSF measured at 170° can simply be extended as constant in that direction. The result is

$$\beta_{\text{ext}}(\psi) = \begin{cases} F_{11,\text{HG}}(\psi) \left[\frac{\beta(10^\circ)}{F_{11,\text{HG}}(10^\circ)} \right], & 0^\circ \leq \psi \leq 10^\circ \\ \beta(\psi), & 10^\circ < \psi < 170^\circ \\ \beta(170^\circ), & 170^\circ \leq \psi \leq 180^\circ. \end{cases} \quad (6)$$

The error of the VSF relative to scattering is then

$$\epsilon_b = \frac{2\pi \int_0^\pi \sin(\psi)\beta_{\text{ext}}(\psi)d\psi - b_{658}}{b_{658}}. \quad (7)$$

VSFs constructed with Eq. (6) from the experimental data, obtained with the MASCOT at 10° intervals from 10° to 170° are displayed in Fig. 3 alongside their relative errors. But because, as predicted, these errors are quite large, the $F_{11,\text{ext}}$ passed to RayXP is not simply $\beta_{\text{ext}}/b_{658}$. Instead, it is corrected for the error

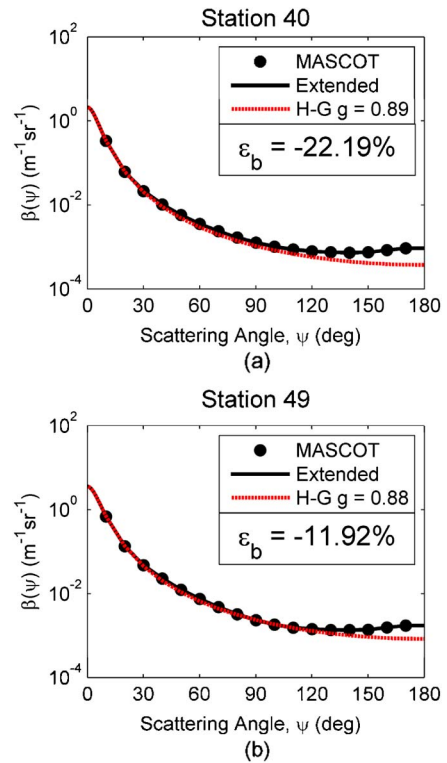


Fig. 3. Volume scattering functions, $\beta(\psi)$, for the two sites. (a) Station 40 and (b) Station 49.

$$F_{11,\text{ext}}(\psi) = 4\pi \frac{\beta_{\text{ext}}}{b_{658}} (1 - \epsilon_b) \quad (8)$$

with the constant 4π required by RayXP. The integral of this extended phase function does not differ from unity by more than 7% as long as the relative error between the integral of VSF and b_{658} is below 30%.

Equipped with polarizers, the MASCOT also measures F_{12}/F_{11} at 10° intervals between scattering angles of 10° and 170° . Implementing these measurements in the simulations is crucial; the alternative is the model of Rayleigh scattering, a default in RayXP, but Fig. 4 shows that F_{12}/F_{11} is not necessarily peaked at 90° , as Rayleigh theory predicts, but closer to 100° . As with the phase function, the ratio must be extended to 0° and 180° , but this time three separate curve fittings are conducted for each station: two power laws for the extension and Rayleigh theory to complete the scattering matrix.

F_{12}/F_{11} must never change in sign, and its bell shape must be anchored at 0 at 0° and 180° . Power laws of the form $y = a_1(x - a_3)^{a_2}$, where each a_i is a constant, are therefore ideal for extending the ratio to all scattering angles. The constant a_3 can be set to any desired value at which y must reach 0, and a_1 and a_2 can then be computed by a simple nonlinear least squares fit. Of course, F_{12}/F_{11} , being a bell, resembles a power law only in sections, specifically for scattering angles where it is concave up, by the sign convention of Fig. 4. The last four positive data points from each end—forward and backward scattering—suffice for the fit. And once the constants

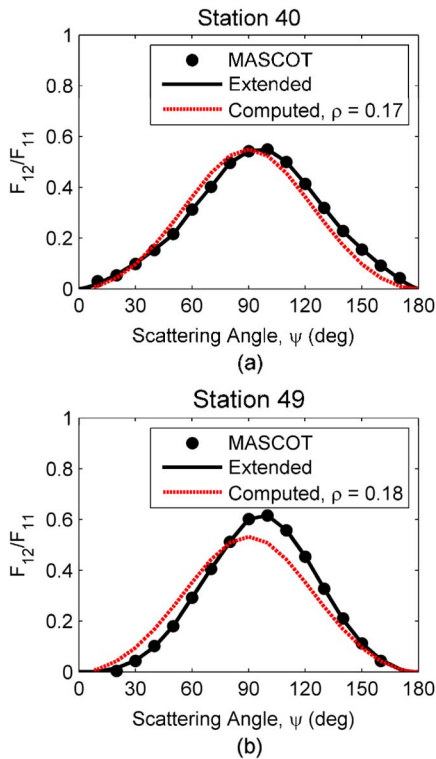


Fig. 4. Extending and fitting the measured ratio F_{12}/F_{11} for two sites. (a) Station 40 and (b) Station 49. The extended functions are used to execute simulations with RayXP. The depolarization factor ρ , which characterizes the fit, also is used by RayXP to solve the equations of Rayleigh scattering for the F_{22} , F_{33} , and F_{44} elements of the scattering matrix.

a_1 and a_2 are known, the power law can be solved over $0^\circ \leq \psi \leq 10^\circ$ and $170^\circ \leq \psi \leq 180^\circ$ and then appended to the measured F_{12}/F_{11} . The extended ratio can then be multiplied by the extended phase function $F_{11,\text{ext}}$ described before to reveal the F_{12} component of the scattering matrix.

The equations of Rayleigh scattering implemented in RayXP are used to complete the scattering matrix, the remaining diagonal elements not being measured. Their governing parameter is ρ , the depolarization factor [29], which can be obtained by fitting the measured F_{12}/F_{11} with the analytic [30]

$$\left(\frac{F_{12}}{F_{11}}\right)_a = -\frac{(1-\rho)(\cos^2\psi-1)}{(1+\cos^2\psi)+\rho(3-\cos^2\psi)}. \quad (9)$$

Because of the shift in the scattering angle at which F_{12}/F_{11} attains its maximum, a perfect fit is impossible, but it is only intended to preserve the shape of the measurements. It is an effective approximation necessary for determining the F_{22} , F_{33} , and F_{44} elements of the scattering matrix.

The parameters of phase matrices along with the main metadata conditions for the stations of study are presented in Table 1.

C. Bottom Layer: Benthic Reflectance

Benthic surfaces are assumed to be perfectly level, homogeneous, and Lambertian. Plants are certainly not flat, but since a near-surface down-looking sensor perceives not individual leaves but rather a weighted average of all benthos in a single plane, the bottom can be modeled as effectively flat and evenly mixed [9]. A Lambertian bottom, or one that reflects light equally in all directions and therefore appears independently of viewing angle, is more of an idealization, but it can readily be applied to real surfaces. Replacing a non-Lambertian bidirectional reflectance distribution function (BRDF) with a Lambertian one introduces errors of approximately 10% in the calculation of the actual normalized radiance [9,31]. Hedley *et al.* [32] have reported that the strongest nonisotropic reflectance is associated with denser longer-leaved canopies, which impacts on near-surface radiance, can be greater than 10%.

The reflectance of each benthic constituent, or “target,” is calculated for this study as the ratio of the radiance reflected from the target into the fiber-optic probe of the DiveSpec (NightSea) to the radiance reflected from a 99% Spectralon reference held at the same depth as the target. This ratio is equivalent to the irradiance reflectance if the target is assumed to be Lambertian [33]. For each target, approximately three to five field measurements were averaged and smoothed with a five-point moving median. At coral reefs, targets consisted of sponges, gorgonians, live corals, carbonate hard-bottom platform, and detritus. Sea grass beds included canopies, individual leaves, and other substrates. To establish the relative contribution of each target to the overall benthic reflectance at a given site, RGB photographs were taken of the area directly beneath the polarimeter. This study analyzes the images with ENVI software (EXELIS Visual Information Solutions). Representative band ratios for each of the most relevant targets are identified through RGB channels and then used to measure percent cover (as pixel count per photograph) for the site. The benthic reflectance is computed as the mean of all target spectra, with each component weighted by its percentage in the total cover.

Small variations in the bottom and movement of the vessel with the currents and wind could cause differences in the readings of the fiber-optic probe near the target and the corresponding radiances measured with the polarimeter, which sensors were typically 1 m below the water surface. Moreover, different water depths create differently sized benthic footprints contributing to the near-surface radiance that are not always represented by the mixtures retrieved from the bottom photographs. Such errors should be incorporated in any analysis of radiance in this paper, and typical benthic reflectances were taken from the software package Hydrolight [34] to facilitate visual assessment of the realism of the measurements.

4. Comparison of the Measured and Simulated Polarized Light Fields in Deep Water (Station 40)

Station 40 (N 24°43.154, W 80°50.005), with a depth of 18 m, represents the site of greatest depth in this study. A reef of white, brown, and gray coral, visible from the research vessel, rose 3 m above the sand-covered seafloor. The benthic reflectance of this station is determined by comparing simulations in the scalar mode with the radiometric measurements by the down-looking polarimeter at 1 m below the surface. Simulations of the hyperspectral I component, the DoLP, and the AoLP are then compared to their measured counterparts. Shallow stations are analyzed in similar fashion in Section 5.

A. IOPs

The water column at this station was uniformly clear; a and c , displayed in Fig. 5, are relatively low in all visible light and virtually constant over all depths. Because of such clarity, light reflected from the seafloor could easily reach sensors at the surface of the water. And this study is most interested in elucidating the effects of the seafloor.

B. Benthic Reflectance

Even though this station is quite deep (18 m), it is optically shallow where the benthic reflectance contributes to the near-surface radiance field. The magnitude of the benthic reflectance can vary threefold across a region, depending on the amount of organic matter found on the surface of any sediments [35]. Reflective properties of corals also vary, depending on the type and health of the reef system, but they generally exhibit distinct features at 573, 604, 652, and 675 nm [36]. Figure 6(a) shows that the radiance simulated with the default Hydrolight bottom in

Fig. 6(b) overwhelmingly exceeds the measured radiance.

The upwelling radiance in Fig. 6(a) and all analogous figures in Section 5 is simply the I component at a 90° instrument angle (at 1 m depth) normalized by the downwelling irradiance. Measurements are, of course, normalized by measurements, and the I from RayXP is normalized by E_d from Eq. (4).

Two simulations appear to match the measurements of radiance very well in Fig. 6(a), but only locally. Based on the measured benthic reflectance, the simulated radiance is excellent between 400 and 520 nm, but between 520 and 580 nm, no bottom at all is best. Above 600 nm, the radiances are difficult to distinguish because of the high attenuation of red light by water. Numerically, it would therefore be best to splice a more strongly absorbing bottom into the measured reflectance between 520 and 700 nm. Doing so would not be realistic, however, because of the aforementioned spectral features definitive of coral. Therefore, the measured benthic reflectance is used to simulate polarized radiance in RayXP. Its partial similarity to a hypothetical infinite depth is a potential source of error.

C. Radiance Field

Upwelling radiance was measured with the polarimeter and later simulated with RayXP for a fixed instrument depth of 1 m, varying scattering planes, multiple wavelengths between 400 and 700 nm, and the entire hemisphere of downward instrument angles. The multidimensional datasets for light 15° from the principal scattering plane are displayed in Fig. 7. The two simulations are consistent with the bottoms described in Section 4.B; the absence of a bottom is synonymous with infinite depth, and the

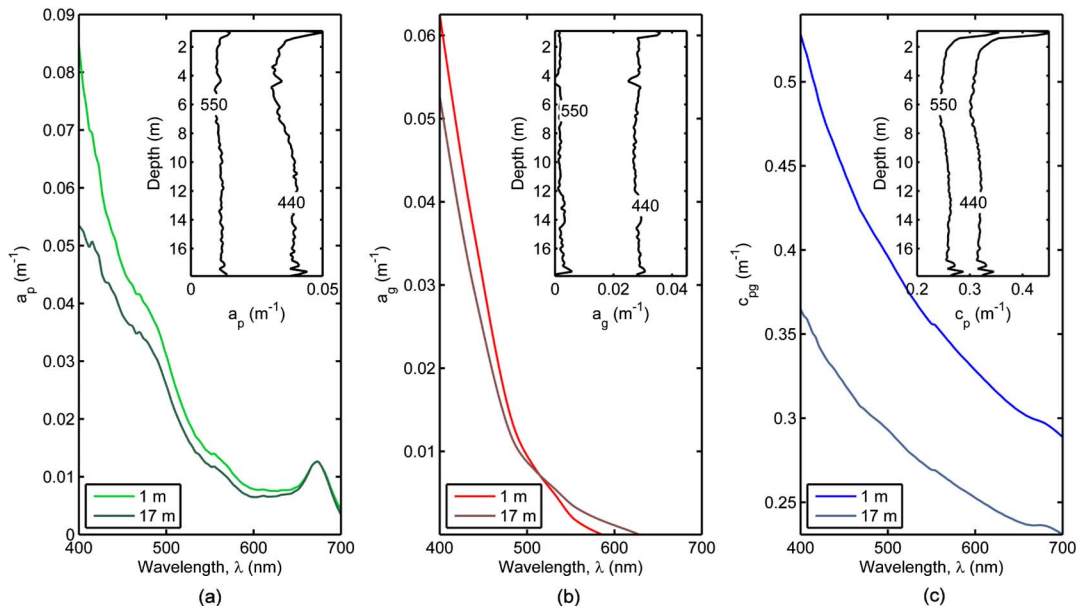


Fig. 5. Spectral plots of IOPs with insets showing depth profiles for 440 and 550 nm. (a) Absorption coefficient of suspended particulate matter, denoted with a subscript p . (b) Absorption coefficient of colored dissolved organic matter (CDOM), also called *gelbstoff*, denoted with the subscript g . (c) Combined attenuation coefficient of suspended and dissolved matter, denoted by pg .

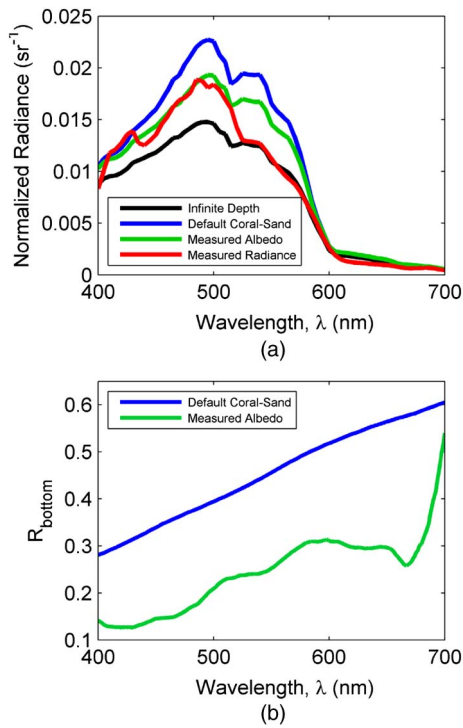


Fig. 6. Normalized radiances are displayed in panel (a) as measured, as simulated with an infinite depth—which is equivalent to the absence of a bottom—and as simulated with the two benthic reflectances of (b). Curves in (a) are labeled either as measurements or based on the benthic reflectance used to simulate them. These same benthic reflectances are used to label (b).

radiance simulated with the measured benthic reflectance slightly exceeds the measured radiance at 550 nm but is otherwise very similar to it. Here and below there are two horizontal axes: the instrument angle explained in Fig. 1 and the scattering angle (more details are provided in Fig. 9).

More conspicuous than the expected differences between the simulations shown in Fig. 7 are the similarities. Regardless of the presence of a bottom, the radiances are of the same order of magnitude and

exhibit the same shape over all instrument angles in yellow and red light. Furthermore, the radiance there is *higher*, even without a benthic reflectance, than measured. A possible reason is the lack of sunlight in the backward-viewing direction, from 90° to 180° , in the shadow the polarimeter cast under an afternoon sun. This shadow reduced the measurements of radiance but could not be incorporated into the simulations. In the forward-viewing direction, where there was still direct sunlight, the seafloor actually contributed considerably to the upwelling radiance; its full effect, if not evident in Fig. 7, is quantified in Section 4.E.

D. Polarization

The fact that the radiance of upwelling light increases due to the presence of a bottom already suggests that bottom is depolarizing; as I intensifies, Eq. (2) states that DoLP should fall, as long as the other Stokes components, namely Q and U , do not rise even faster, as in a polarizing medium. Figure 8 indicates that in this particular station, they are stable, and that the bottom is indeed depolarizing. The hyperspectral, multiangular plots are constructed just as in Fig. 7, and through them the simulations qualitatively reveal that the polarization of light in the water column is partially reversed by benthic reflections. The simulations without benthos show essentially what happens in pure water. As myriad beams of light are repeatedly scattered by water molecules, they align in distinct directions, and thus they are collectively deemed polarized. But when the beams fall incident upon a bottom of coral and sand, their alignment is perturbed, and they are reflected upward unpolarized. Thus the total upwelling radiance must increase, but the fraction of polarized light within it must decrease—all because of the seafloor. The seafloor effectively dilutes the polarization in water in a larger pool of light.

In general, the peak and indeed the behavior of the DoLP depend on the single scattering albedo ω ,

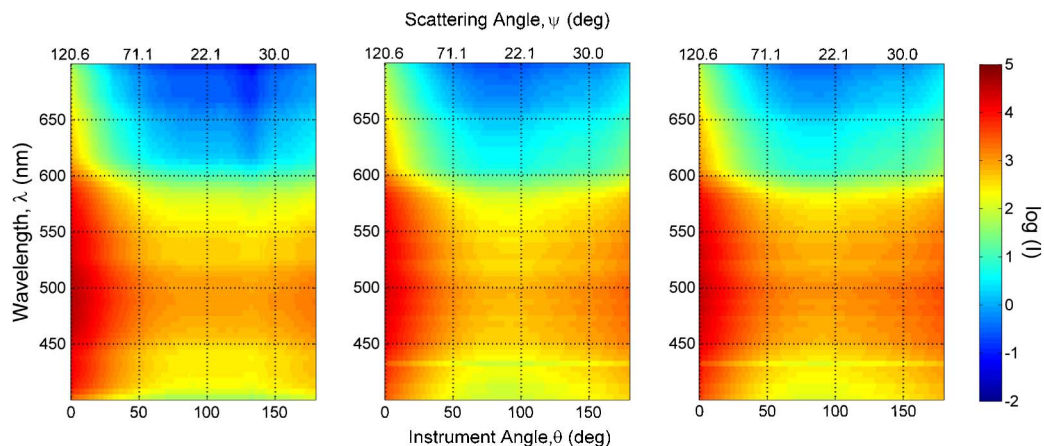


Fig. 7. Stokes component of radiance (I), presented hyperspectrally and for all downward-looking instrument angles 15° from the principal plane. From left to right: measurements, vector RT simulations of an ocean with effectively no bottom, and vector RT simulations of an ocean with a realistic bottom.

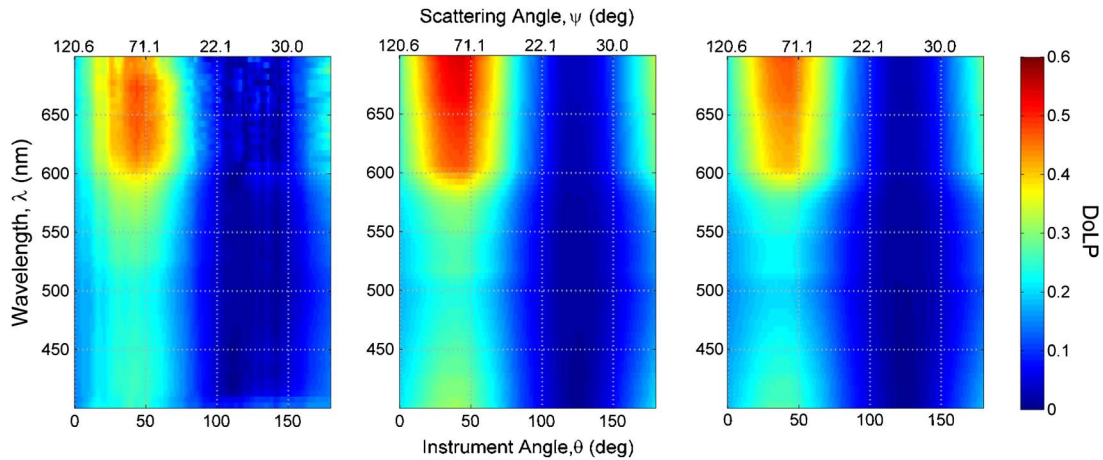


Fig. 8. DoLP, presented hyperspectrally and for all downward-looking instrument angles 15° from the principal plane. From left to right: measurements, vector RT simulations of an ocean with effectively no bottom, and vector RT simulations of an ocean with a realistic bottom.

as indicated in Eq. (1), or the similar attenuation-to-absorption ratio [37]. With a relatively gradual spectral change of the attenuation coefficient, the DoLP usually increases with absorption because the number of scattering events decreases. In clear water, the total absorption coefficient (the sum of particulate, CDOM, and pure water absorption) is highest in the red part of the spectrum due to the high pure water absorption. There the DoLP has the highest values. Furthermore, the DoLP in this part of the spectrum is better preserved because the bottom effects are well attenuated and do not propagate to the surface. Effects similar but more subtle are seen in the blue part of the spectrum, where CDOM and particulate absorption increases.

In the measurements and in both simulations, the DoLP peaks at different magnitudes—only simulations with the bottom fully match measurements—but at the same instrument angles between 30° and 40° . Based on the geometry shown in Fig. 9 and the solar elevation angle from Table 1, the corresponding range of scattering angles is 84° – 94° . This range conforms with the 90° at which pure water is known to exhibit maximum polarization [18] and incorporates the possible shifts in the F_{12} component of the scattering matrix, explained in Section 3.B.

The AoLP of light propagating out of the principal plane can indicate the orientation of the e-vector, which has implications in biology. It is shown for 45° from the main plane in Fig. 10 in plots analogous to those in Fig. 8. Not surprisingly, there is no significant difference between simulations with and without a bottom. According to Eq. (2), the AoLP depends only on Q and U , neither of which is impacted by benthic reflectance, since Q , U , and V are all zero from a Lambertian surface.

E. Error Analysis

Shown with a relative color scale over the spectral and geometric dimensions, the simulations of DoLP replicate the measurements well, regardless of the presence of a realistic bottom. Here, this comparison

is expressed numerically. Two-dimensional correlation coefficients are computed between each of the simulations and the measurements for each of the Stokes components as well as the DoLP. The R -square (R^2) values are presented in Table 2. They indicate how closely simulations and measurements adhere to the same trend, but they can be misleading. Through them, measurements of DoLP appear more correlated with simulations without the bottom ($R^2 = 0.94$) than with those that include the bottom ($R^2 = 0.93$). And both simulations do follow the same trend as the measurements; Fig. 7 suggests that the values of the three datasets rise and fall in the same general regions. But while they vary similarly, they do not vary across the same values. Simulations without a bottom exceed the measurements more often than those with a bottom. This observation is quantified in the linear regression below.

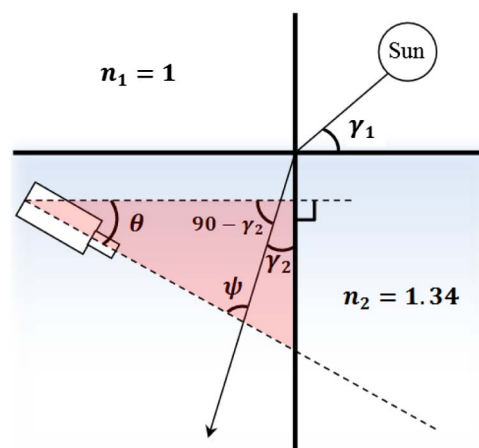


Fig. 9. Angle ψ at which pure water scatters light most strongly and thus causes the DoLP to peak can be computed from the solar and viewing geometry. If the sun is at an elevation angle γ , quantified in Table 1, light will enter the water at γ_2 , in accordance with Snell's Law of Refraction, $n_1 \sin(90 - \gamma_1) = n_2 \sin \gamma_2$. The triangle indicated in red then reveals that $\psi = \gamma_2 - \theta + 90^\circ$, where θ is the instrument angle.

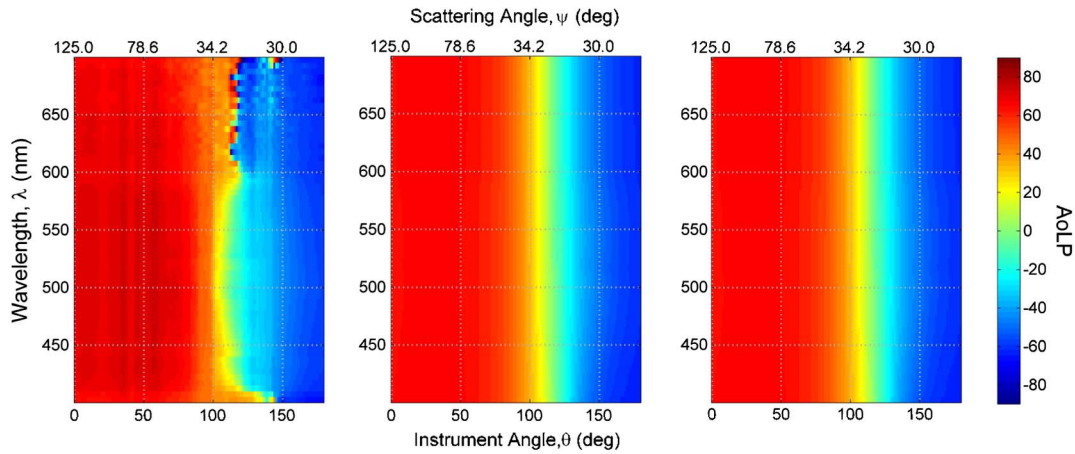


Fig. 10. AoLP based on the Stokes vector 45° from the principal plane, presented hyperspectrally and for all downward-looking instrument angles. From left to right: measurements, vector RT simulations of an ocean with effectively no bottom, and vector RT simulations of an ocean with a realistic bottom.

Table 2. Regression Coefficients for Simulations and Measurements on the 15° Scattering Plane

Simulation	DoLP			I			Q			U		
	R^2	m	b	R^2	m	b	R^2	m	b	R^2	m	b
W/Bottom	0.928	0.999	-0.016	0.979	0.910	0.165	0.979	0.851	-0.023	0.570	0.703	-0.046
No Bottom	0.941	1.124	-0.009	0.982	0.787	0.108	0.979	0.849	-0.024	0.571	0.703	-0.046

For simulations to match reality, and thereby indicate whether the bottom is depolarizing, they must exhibit a one-to-one relationship with measurements. The hyperspectral, multiangular data points of the Stokes components and the DoLP are therefore collected into vectors, and a least-squares linear regression of the form $Y = \alpha_1 X + \alpha_0$ is executed between measurements Y and each set of simulations X . The DoLP is scattered about the one-to-one line in Fig. 11, and the regression between the simulations with bottom and the measurements is almost parallel to it, albeit with a slight bias. Without the bottom, simulations of DoLP significantly deviate from the measurements at high values. This divergence is caused entirely by the I component, which in turn is highly sensitive to benthic reflectance. The regression coefficients reported in Table 2 indicate that I without the bottom is much too low, the slope being 0.79; the measured seafloor raises the slope to a more reasonable 0.91. The other Stokes components are not affected by the bottom in accordance with the Lambertian model. Additional correlation and regression coefficients are reported in Table 3 for simulations 45° from the principal plane.

Altogether, the error analysis confirms that the RT model must incorporate a bottom to replicate measurements; that the DoLP without a bottom exceeds that caused by reflection from a bottom, and therefore that the realistic bottom of this station of clear, deep water is depolarizing. The following sections discuss stations that were closer to shore, where both particles and geometry diminish optical depth and could alter polarization.

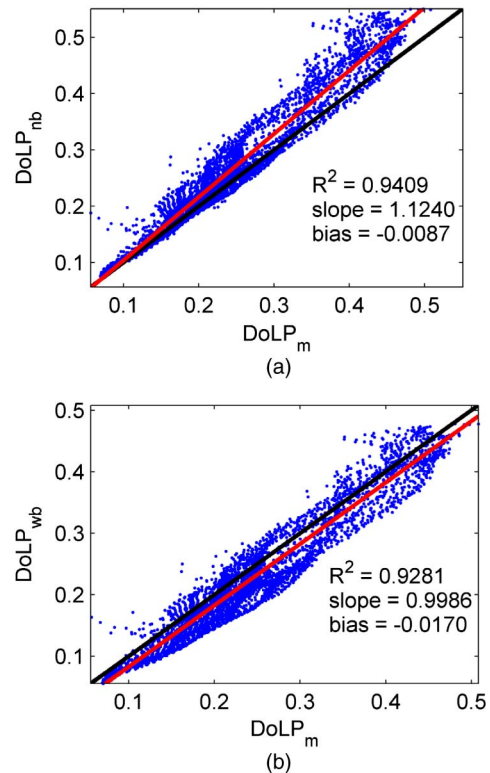


Fig. 11. Measurements of the DoLP, denoted by the subscript “m,” are scattered against simulations with no bottom (“nb”) in (a) and against those with a bottom (“wb”) in (b). The one-to-one lines are shown in solid black and the actual regressions in red.

Table 3. Regression Coefficients for Simulations and Measurements on the 45° Scattering Plane

Simulation	DoLP			I			Q			U		
	R^2	m	b	R^2	m	b	R^2	m	b	R^2	m	b
W/Bottom	0.953	0.845	-0.002	0.978	0.916	0.169	0.975	0.670	-0.010	0.976	1.002	0.016
No Bottom	0.954	0.944	0.010	0.982	0.788	0.115	0.975	0.668	-0.010	0.976	1.001	0.017

5. Comparison of the Measured and Simulated Polarized Light Fields in Shallow Water

This study now proceeds by presenting three stations with shallow water but varying IOPs and benthos; the conditions in each station could have different effects on polarization. Station 49, the first to be presented, is the archetype of coastal waters: it is of intermediate 5 m depth, relatively turbid, and over a bottom of sand and marine grass (sea grass). There, as numerous scattering events polarize light, the depolarizing effect of the bottom is most pronounced. Station 36 was studied under a similar solar elevation, and it also contains a bottom of sea grass, albeit a different species, but being much shallower and clearer, it is characterized by a much lower optical depth. Its DoLP is thus found to be much lower than that of Station 49 but just as sensitive to the benthic reflectance. The final station, 30, is as clear and deep as 49, but its seafloor contains different benthos. These idiosyncrasies are presented, but their effects on polarization are left out of this paper for the sake of brevity. Otherwise, this section is structured like Section 4. An additional subsection—of detailed comparisons between simulations themselves and between simulations and measurements of AoLP and DoLP for specific wavelengths and viewing geometries—is included for Station 49, where measurements were the least noisy and conditions were typical of coastal waters.

A. Station 49: Sand with Sparse Sea Grass, 5 m Depth

The sea grass *Thalassia testudinum* at Station 49 (N 24°43.553 W 80°51.505) was short and sparsely distributed across the white carbonate sediment seafloor. In Fig. 12, the photograph shows the relative contribution of sea grass leaves and bright sediment used in the benthic reflectance. Similar photographs were collected at the other stations but are not shown in this paper for the sake of brevity.

1. IOPs.

The optical properties vary considerably throughout the water column of this station, with the absorption and scattering being higher near the surface (Fig. 13). Within the first meter from the surface, the absorption spectrum steeply decays from blue to red light, a pattern characteristic of nonalgal particles. Particulate absorption decreases below 1 m, leaving the spectral signature of chlorophyll-containing phytoplankton. Absorption by CDOM is relatively constant throughout the water column [Fig. 13(b)].

2. Benthic Reflectance

The contribution of sea grass to sediment varies from 25% to 50% across the site, as shown in Fig. 12. Agreement between measured and simulated upwelling radiance is closest with a benthic mixture of 50% sediment and 50% sand [Fig. 14(a)]. The high reflectance from the white sand increases the measured benthic reflectance considerably from one produced only by sea grass [Fig. 14(b)]. The measurements are implemented in the simulations with RayXP. Note that the upwelling radiances are not actually taken vertically for Fig. 14. Shadows of the research vessel, previously mentioned in the discussion of Station 40 (see Section 4.C), appeared under the instrument, so radiances at instrument angles up to 10° from the vertical are used for the analyses of benthic reflectance in this and subsequent stations.

3. Radiance Field

Upwelling radiance in deep water, as in pelagic environments, is caused entirely by the scattering and reflection of the water and its suspended matter. The contribution of bottom reflection was already evident in Station 40, which was deep but clear. Here, the water is relatively shallow, and so, even with strong attenuation of red and violet light, the effect of the bottom is much more pronounced. The benthic average is clearly responsible in Fig. 15 for elevating simulated upwelling radiance from an arrant underestimate to the measured level. Only at instrument angles of 90° and 130° is the measured radiance slightly indented while the simulated is not, probably because the shadows on the seafloor could not



Fig. 12. Mixture of turtle sea grass and sand from which the benthic reflectance was retrieved for Station 49.

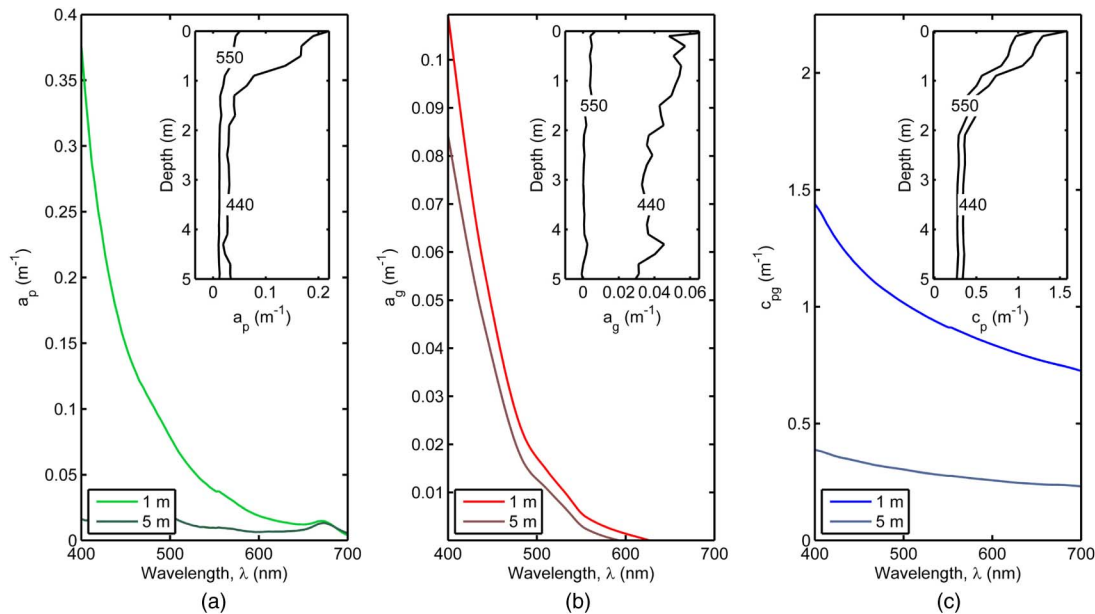


Fig. 13. Spectral plots of IOPs with insets showing depth profiles for 440 and 550 nm. (a) Absorption coefficient of suspended particulate matter. (b) Absorption coefficient of colored dissolved organic matter (CDOM). (c) Combined attenuation coefficient of suspended and dissolved matter.

be implemented in what is still a general model of RT.

4. Polarization

Sea grass and sand comprise a depolarizing bottom. Simulations without it exhibit a realistic pattern in

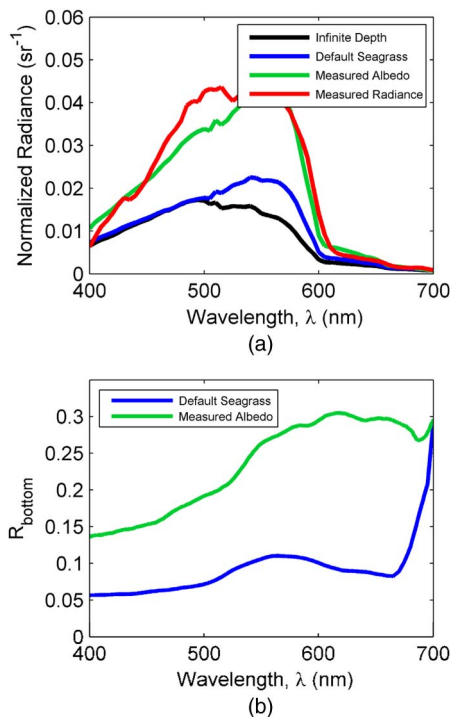


Fig. 14. Normalized radiances are displayed in panel (a) as measured in the field, as simulated with infinite depth—which is equivalent to the absence of a bottom—and as simulated with the two benthic reflectances presented in (b): a default sea grass leaf and the measured mixture of sea grass and sediment.

Fig. 16, the polarization being highest in dim red light and lowest in the brightness of green, but overall this polarization is much higher than what was measured. Only the bottom reduces it—depolarized light—to a level that matches the measurements. The reduction is much sharper for all wavelengths in this shallow station than in the relatively deeper Station 40, and it is probably more representative of benthic effects on polarization. For in deep water, photons reflected from the bottom lose information as they propagate upward, especially in the 600–700 nm range. In a shallower water column that is mostly clear, all the green and even the yellow light reflected by the benthic sand and sea grass reaches sensors at the ocean surface and conveys information about depolarization.

The presence of the bottom is detectable at the surface also through the patterns in the scattering angle of maximum polarization. In red light, attenuation due to water predominates regardless of the bottom. The viewing angle of maximum polarization in this spectral band is 44° . In accordance with the geometry of Fig. 9, the corresponding scattering angle is $\psi = 90 - 44 + \sin^{-1}(\sin(90 - 28)/1.34) = 87^\circ$, which is very close to the 90° exhibited by pure water. Without the bottom, water continues to exert the strongest effect on polarization at other wavelengths, keeping the viewing angle of the polarization peak around 45° . But when green and yellow wavelengths of light are reflected from the benthos, as in the simulations and in reality, the DoLP almost entirely vanishes at this geometry and peaks instead at 32° or a scattering angle of 99° . Evidently the seafloor not only increases radiance but accentuates its dependence on scattering in the water column.

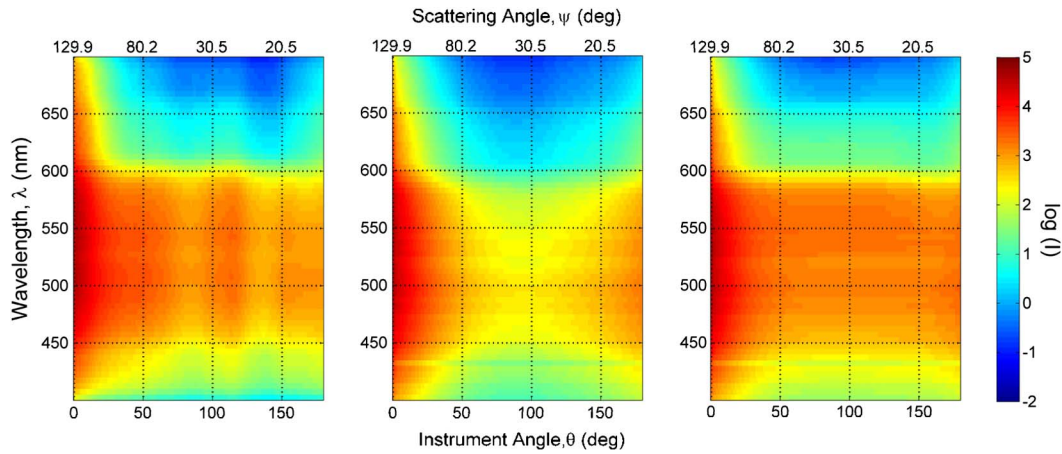


Fig. 15. Stokes component of radiance (I), presented hyperspectrally and for all downward-looking instrument angles 15° from the principal plane. From left to right: measurements, vector RT simulations of an ocean with effectively no bottom, and vector RT simulations of an ocean with a realistic bottom.

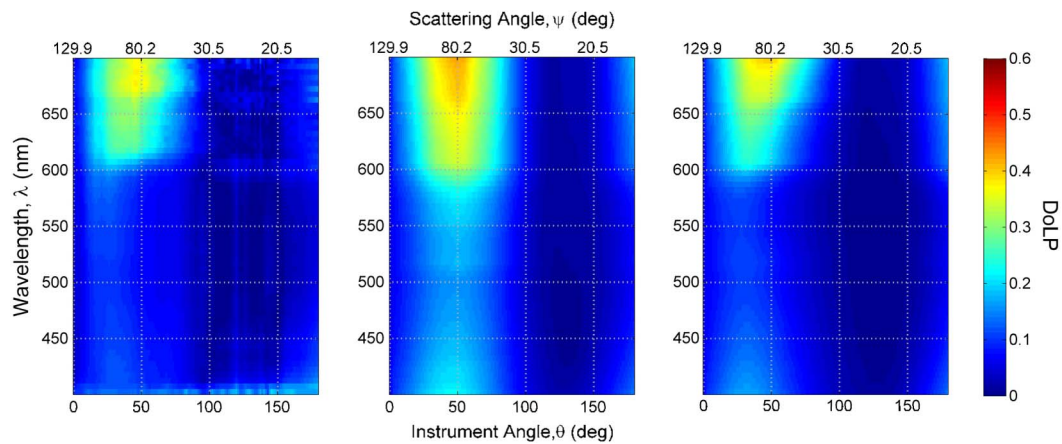


Fig. 16. DoLP, presented hyperspectrally and for all downward-looking instrument angles 15° from the principal plane. From left to right: measurements, vector RT simulations of an ocean with effectively no bottom, and vector RT simulations of an ocean with a realistic bottom.

As discussed in Section 4.D in the case of deep water, the seafloor does not affect AoLP. Even if it slightly changes the values of the Stokes elements Q and U , these changes cancel out when their ratio is computed in Eq. (2). The measured and the simulated AoLP exhibits a similar pattern as in Station 40 in Section 4.D above.

5. Error Analysis

Noise from the environment, such as diffuse light, in measurements of a specific target, in this study the seafloor, inevitably disperse data from a perfect, analytical trend. Noise especially pervaded measurements of this station in instrument angles between 90° and 180° . Nevertheless, the scatterplots of Fig. 17 indicate that simulations with the bottom match the field measurements almost perfectly; the regression is one-to-one with minimal spread ($R^2 = 0.94$) and bias. Without the bottom, the correlation is weaker ($R^2 = 0.78$), the trend is skewed by the change in the maximum scattering angle over 500–600 nm (explained in Section 5.A.4), and the bias is more than 10 times higher due to the lack of benthic

reflections in the upwelling light. The regression is clear evidence that the seafloor is depolarizing, and the correlation that it reshapes the polarized light field as it accentuates scattering.

Correlation and regression coefficients for the Stokes components are presented in Tables 4 and 5 as they were for the deep water station. The seafloor improves I just like it did there. But whereas it appeared to have virtually no effect on Q and U in deep water, the coefficients for these components do change between the simulations in Table 4. They are not altered by the bottom itself; polarized radiance is independent of Lambertian reflectance. Instead, they are probably intensified by the bottom and changed by scattering in the water column.

6. Detailed Qualitative Comparison of Measurements and Simulations

Polarization—both its magnitude and direction—is examined for this station for specific wavelengths (440, 550, and 665 nm) and viewing geometries (horizontal, peak scattering, and vertical). The polarization in pure water peaks at 90° scattering angle,

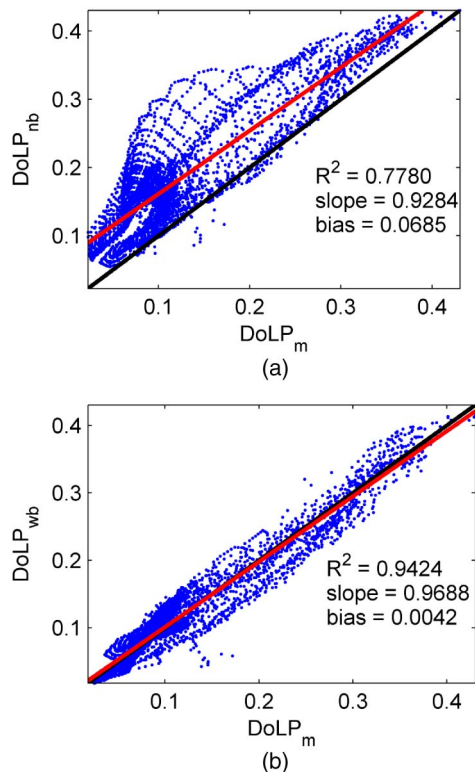


Fig. 17. Measurements of the DoLP, denoted by the subscript “m,” are scattered against simulations with no bottom (“nb”) in (a) and against those with a bottom (“wb”) in (b). The one-to-one lines are shown in solid black and the actual regressions in red.

so the instrument angle that would intercept directly scattered light is, based on Fig. 9, $\theta = \gamma_2 = \sin^{-1}(\sin(90 - 16.5)/1.34) = 41.22^\circ$. In the red part of the spectrum, the ocean behaves almost as if it were pure water molecules raising the DoLP to its maximum between 40° and 50° in measurements and both simulations. However, peak DoLP in blue and green light was measured at a 32° instrument angle. Only simulations with the bottom match it, those without a bottom remaining closer to 50° . That alone is evidence of the crucial role of the bottom in the marine environment. Figure 18 further validates the with-bottom simulations; at the chosen instrument angles, they almost perfectly overlap the measurements. A slight incongruity does manifest itself even in the presence of the bottom in blue and violet light. Simulations incorporating the benthic average replicate the measurements everywhere but for the 0° – 50° instrument angles at 440 nm in Fig. 19, which is probably due the layer of nonalgal particles in the vicinity of the polarimeter. Otherwise, Fig. 19 confirms that the bottom is depolarizing and shifts the scattering angle at which polarization attains its maximum.

Erratic colors in the AoLP in Fig. 10 for Station 40 and similarly for Station 49 (not shown) at instrument angles above 90° reflect the noise-permeating measurements on the 45° scattering plane. This noise cancels out, however, in the ratio that defines the DoLP, and the corresponding regression

Table 4. Regression Coefficients for Simulations and Measurements on the 15° Scattering Plane

Simulation	DoLP			I			Q			U		
	R^2	m	b	R^2	m	b	R^2	m	b	R^2	m	b
W/Bottom	0.942	0.969	0.004	0.960	0.922	0.090	0.909	0.962	-0.004	0.753	0.727	-0.022
No Bottom	0.778	0.928	0.069	0.911	0.857	-0.265	0.898	0.992	-0.013	0.761	0.743	-0.027

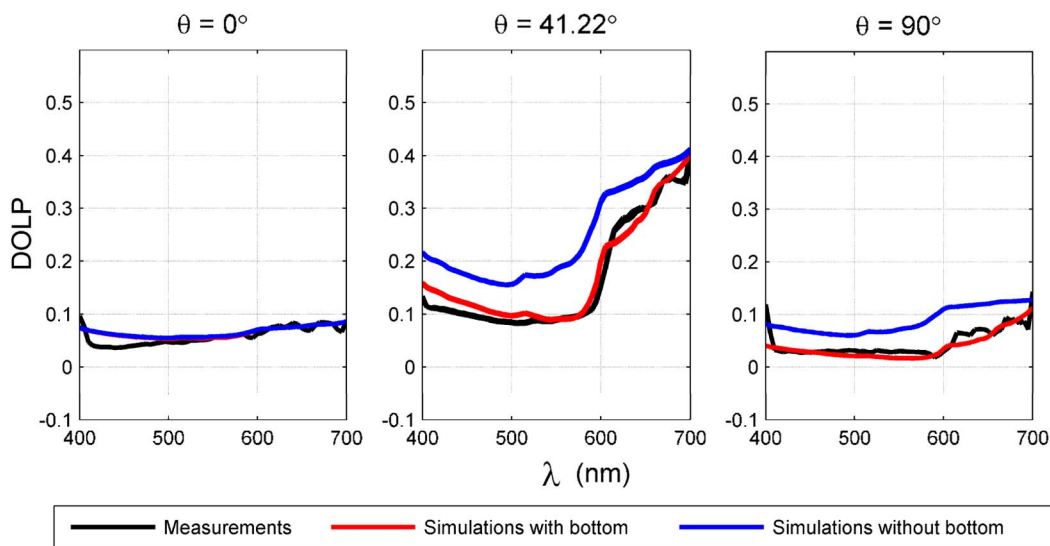


Fig. 18. Spectral plots of DoLP for the three angles at which the polarimeter looks horizontally, in the theoretical peak scattering direction, and vertically, shown in that order from left to right.

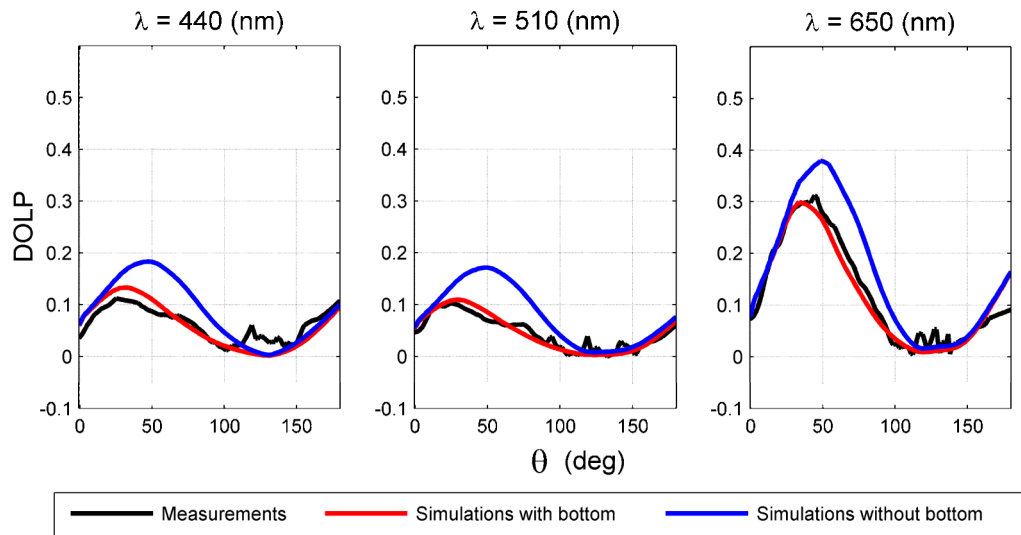


Fig. 19. Angular plots of DoLP for the blue, green, and red channels.

Table 5. Regression Coefficients for Simulations and Measurements on the 45° Scattering Plane

Simulation	DoLP			I			Q			U		
	R^2	m	b	R^2	m	b	R^2	m	b	R^2	m	b
W/Bottom	0.921	1.052	-0.021	0.937	1.197	0.168	0.767	1.104	-0.012	0.909	0.901	0.026
No Bottom	0.684	0.846	0.071	0.873	1.032	-0.118	0.780	1.150	-0.016	0.879	0.903	0.039

coefficients in Table 5 tightly recreate the one-to-one line, but only with the bottom. Similarly, the noise could also be canceled out in the ratio used to compute AoLP. Indeed, the regression line of with-bottom simulations (Y) over measurements (X) of AoLP is of the form $Y = 0.82X + 11.94^\circ$ with correlation strength $R^2 = 0.70$. If the bottom is excluded from the RT model, the equation is $Y = 0.81X + 12.20^\circ$ with correlation strength $R^2 = 0.71$. The similarity of the two regressions indicates that a bottom changes the magnitude of polarization in upwelling light but not the orientation. Figures 20 and 21

validate these claims visually in plots analogous to those in Figs. 18 and 19.

B. Station 36 (Sea Grass, 1.5 m Depth) and Station 30 (Coral, 5 m Depth)

1. IOPs

Station 36 (N 24°52.506, W 80°53.795) contains a dense bed of sea grass consisting primarily of the cylindrical-leaved *Syringodium filiforme*. Although the physical depth of this site is 2 m, the sea grass canopy is approximately 0.5 m high, so the sensors perceived an effective depth of 1.5 m. The water

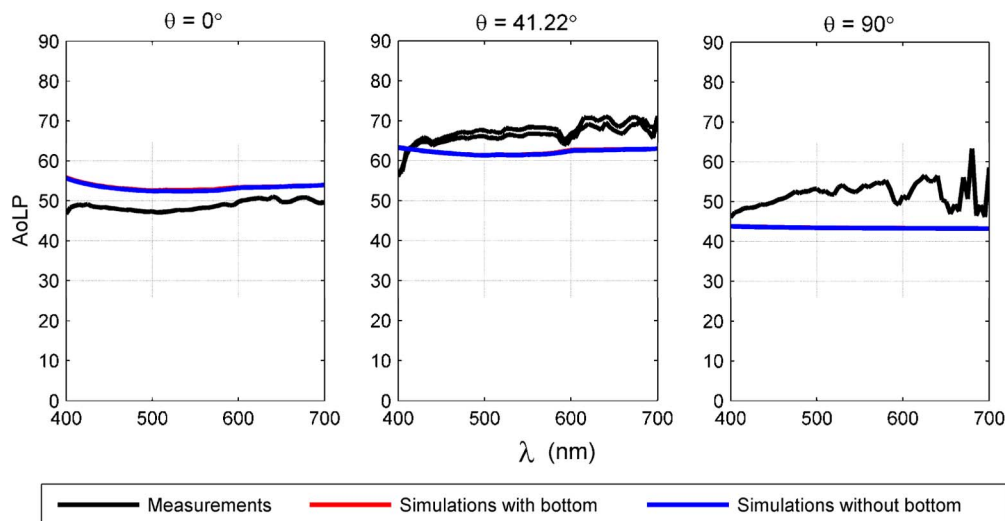


Fig. 20. Spectral plots of AoLP for the three instrument angles explained in the text.

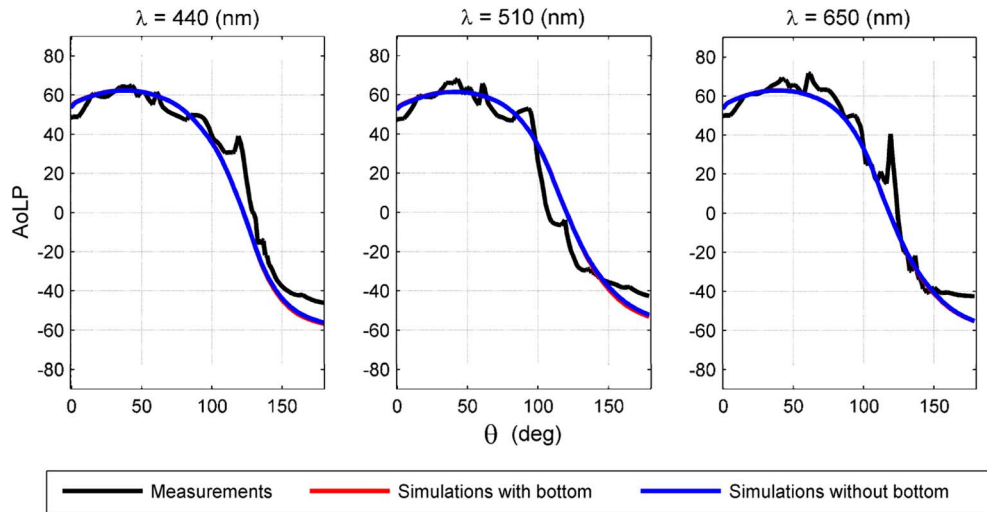


Fig. 21. Angular plots of AoLP for the blue, green, and red channels.

column of this station is turbid; a 400 nm absorption coefficient of suspended particulate matter was about 0.55 m^{-1} , with CDOM absorption about 0.8 m^{-1} and attenuation coefficient about 2 m^{-1} . In contrast to Station 49, these parameters are uniformly distributed from the 0.9 m depth at which the ac-s instrument was immersed to the 1.5 m at which sea grass swayed.

Station 30 (N $24^{\circ}41.555$ W $80^{\circ}56.866$) is discussed briefly in subsection 5.B.6. Other than a bed of coral, it is as deep as Station 49. Its water column is uniform and relatively clear with an absorption coefficient of about 0.6 m^{-1} for suspended particulate matter at 400 nm, a CDOM absorption of about 0.12 m^{-1} , and an attenuation coefficient of about 1 m^{-1} . The resulting radiance and polarization fields therefore are very similar to those presented in the Section 5.A and are not shown in this paper.

2. Bottom Reflectance

Reflectance from a dense sea grass canopy is generally low with a rounded peak in the green portion of the spectrum [35]. The peak is much more pronounced here, as shown in Fig. 22, than in Station 49, where the sea grass was interspersed with bright sediment. To account for subtle fluctuations in canopy height across the station, the measured benthic reflectance is adjusted as shown in Fig. 22(b). That is, the accurate shape of the measurements was biased to match the accurate scale of the default sea grass, but the sharp spike between 650 and 700 nm was removed, as it is clearly not reflected in the radiance, whose measurements are more reliable than those of albedo. The resulting “adjusted albedo” therefore maintains the primary spectral features of the measured reflectance while significantly decreasing the error between the measurements and RayXP simulations of the normalized radiance. It is implemented in the final model for this station.

3. Radiance Field

Simulations with a bottom more closely match the measurements than simulations without it, as shown in Fig. 23. Without a seafloor, they are unrealistically low except at the horizontal instrument angles ($\theta = 0^{\circ}$). At that angle, radiance is determined partly by small contributions from the bottom reflectance and multiple scattering by the hydrosols, but it

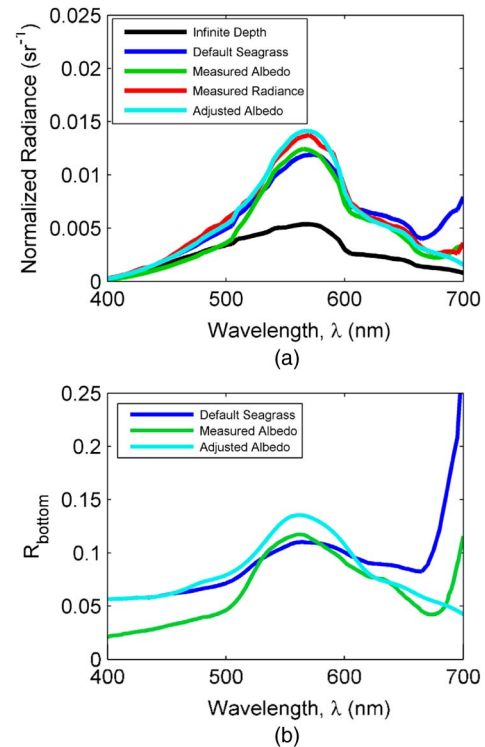


Fig. 22. Normalized radiances are displayed in (a) as measured, as simulated with infinite depth, which is equivalent to the absence of a bottom, and as simulated with the three benthic reflectances of (b). Curves in (a) are labeled either as measurements or based on the benthic reflectance that was used to simulate them. These same benthic reflectances are used to label (b).

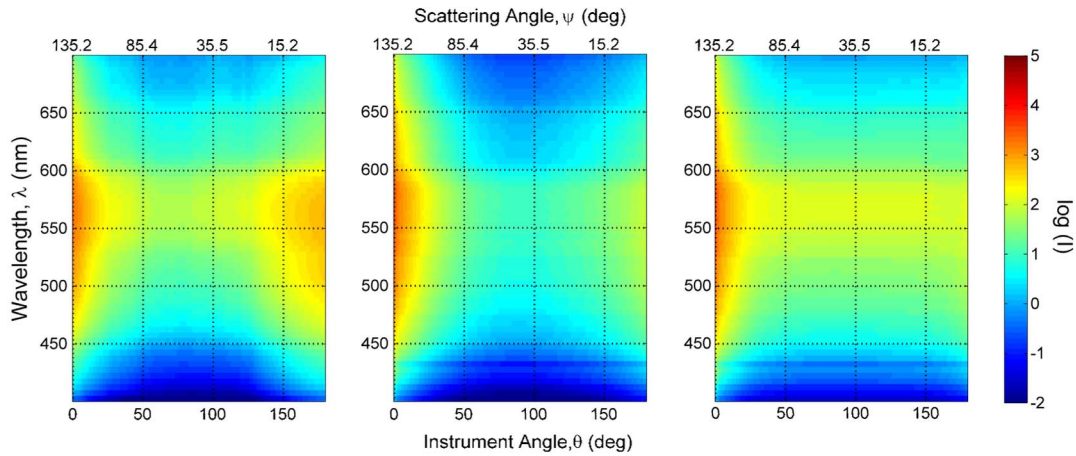


Fig. 23. Stokes component of radiance (I), presented hyperspectrally and for all downward-looking instrument angles 15° from the principal plane. From left to right: measurements, vector RT simulations of an ocean with effectively no bottom, and vector RT simulations of an ocean with a realistic bottom.

is primarily dependent on the IOPs, so *any* simulations of it based on a measured phase function and attenuation should certainly match measurements. Yet in the opposite horizontal direction ($\theta = 180^\circ$), both simulations yield values far below the measurements. The reason is not entirely clear. These effects are exogenous to the experiment and the numerical model, and error analyses in this study are conducted for instrument angles between 0° and 90° anyway. The adjusted benthic reflectance improves the simulations significantly in that viewing geometry; upwelling radiance is clearly highly sensitive to the seafloor in these shallow waters.

4. Polarization

Depolarization due to the seafloor is profound in this shallow station. Levels of DoLP in simulations based on the benthic reflectance are often less than half of those based on the hypothetically infinite depth. These with-bottom simulations are also extremely accurate with respect to measurements. In Fig. 24, they

replicate not only magnitude of DoLP but also its distribution, with peaks in blue and red light and the trough in green where reflections from sea grass are strongest. The instrument angle at which these peaks occur is 27° , which corresponds to a scattering angle $\psi = 90 - 27 + \sin^{-1} \sin(90 - 20.5)/1.34 = 107^\circ$.

5. Error Analysis

Figure 25 quantifies the effect of the seafloor on polarization for Station 36. Simulations without the bottom are strewn above the measurements, while simulations with it exhibit a narrow, one-to-one relationship with them. The incremental bias is most likely a relic of the difficulty of measuring light near the shore in such shallow waters. Table 6 further enumerates the regression coefficients and correlations of simulations over measurements of the remaining Stokes components. The improvement with a bottom in I alone is not enough to account for the dramatic change in DoLP; Q and U improve

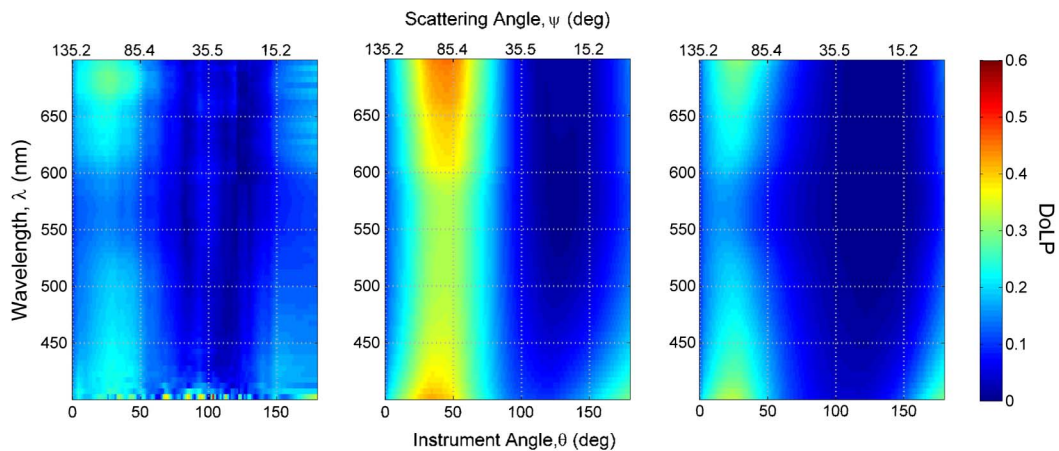


Fig. 24. DoLP, presented hyperspectrally and for all downward-looking instrument angles 15° from the principal plane. From left to right: measurements, vector RT simulations of an ocean with effectively no bottom, and vector RT simulations of an ocean with a realistic bottom.

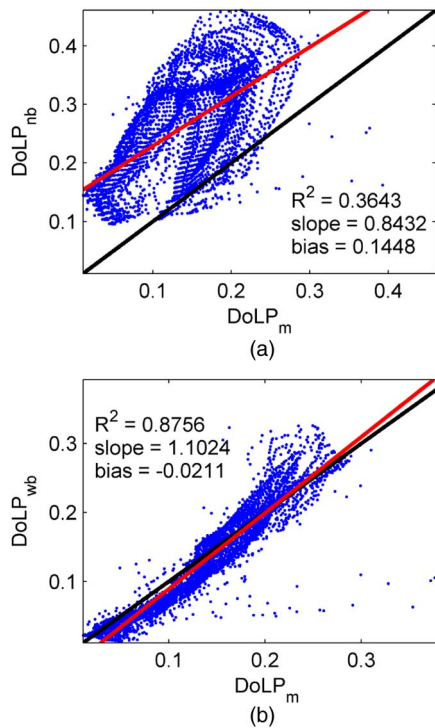


Fig. 25. Measurements of the DoLP, denoted by the subscript “m,” are scattered against simulations with no bottom (“nb”) in (a) and against those with a bottom (“wb”) in (b). The one-to-one lines are shown in solid black and the actual regressions in red.

much more significantly, despite the assumption that the bottom is Lambertian.

6. Station 30

The main features of this station and IOPs were already introduced in subsection 5.B.1. Only retrieval of the benthic average is presented below. This station exhibits relatively high scattering and backscattering (relative to absorption). In a water column, this backscattering can produce considerable upwelling radiance. The simulation of radiance using the Hydrolight default for coral reflectance is lower than the radiance with no bottom at all, as is apparent between 450 and 550 nm in Fig. 26. Benthic reflectance of corals depends on the health of the organism and the amount of sedimentation on the reef. The measured benthic reflectance is at least 0.1 units higher than the default for all wavelengths and increases the simulated radiance at the sea surface. Simulations using the measured albedo still do not mimic the measurements fully, but are adequate for use in RayXP.

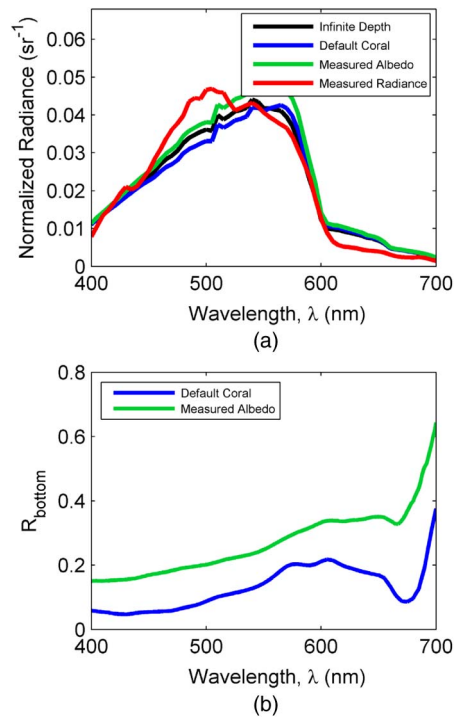


Fig. 26. Normalized radiances are displayed in (a) as measured, as simulated with infinite depth, which is equivalent to the absence of a bottom, and as simulated with the two benthic averages of (b). Curves in (a) are labeled either as measurements or based on the benthic average that was used to simulate them. These same benthic averages are used to label (b).

6. Cumulative Comparison

Underwater polarization varies with the location of the sun in the sky, the concentration of matter suspended or dissolved in the water, and now, as this study has shown, with the reflectance of the seafloor. A cumulative comparison of the significance of these factors is presented in Fig. 27. The DoLP is shown in the plane, which was about 15° from the principal plane over all instrument angles for the blue, green, and red channels. Its dependence on the bottom emerges already in Station 40, where it falls by about 5 percentage points from simulations without the bottom to those that incorporate it. Because the upwelling radiance in the deep waters of that station was partially extinguished before reaching the surface, the DoLP persisted at high levels, above 20% in blue and green light and above 40% in red light. In shallower environments, especially in those of Station 36, the depolarizing effect is more pronounced, dropping DoLP from an average 35% without the bottom to less than 20% with it. The same

Table 6. Regression Coefficients for Simulations and Measurements on the 15° Scattering Plane

Simulation	DoLP			I			Q			U		
	R^2	m	b									
W/Bottom	0.876	1.102	-0.021	0.968	1.102	0.046	0.974	1.107	-0.004	0.703	1.042	-0.003
No Bottom	0.364	0.843	0.145	0.911	1.110	-0.067	0.936	1.287	-0.019	0.807	1.207	-0.007

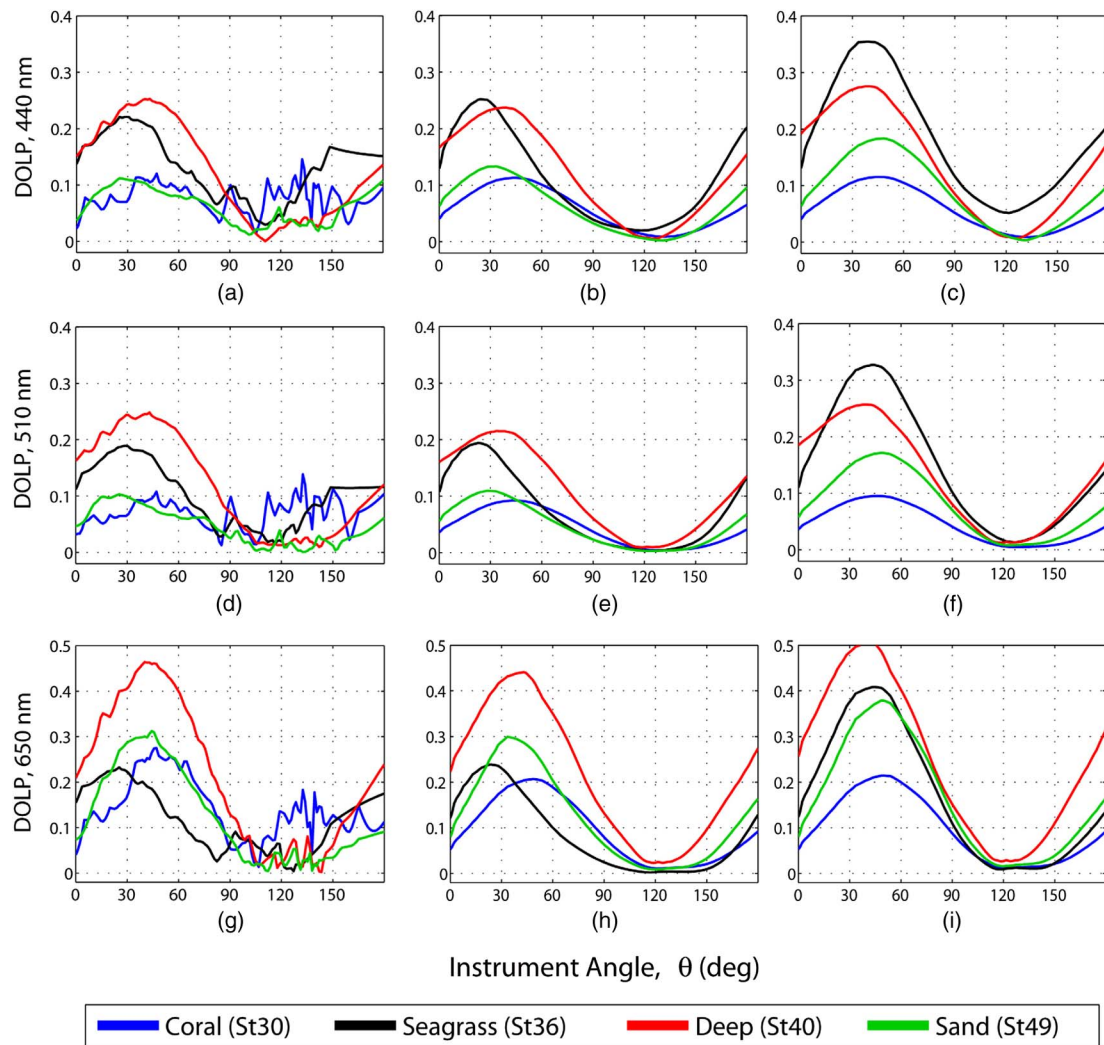


Fig. 27. DoLP as a function of instrument angle at three wavelengths at all studied sites. Left-hand panels: measurements. Center: simulations with bottom effects. Right-hand panels: simulations without bottom effects.

effect can be observed in Station 49 as well. Taking the bottom into account was vital for the establishment of a high correlation and one-to-one regression between simulations and measurements, and it is therefore very likely to be present in nature.

Biological implications of a depolarizing bottom are interesting, particularly in terms of camouflage. Benthic organisms could customize their camouflage strategies to the unique features of their environs. For example, octopi and bottom-dwelling fish can adopt depolarizing reflectance properties. In contrast, camouflage becomes more challenging for organisms, such as silvery fish [38], which occupies the water column above the benthos in shallow waters. These organisms would require a two-pronged strategy dependent on their predator's viewing plane. They would have to exhibit unpolarized reflectance on their dorsum to hide from predators viewing them from above while maintaining polarized flank reflectance to hide from predators viewing them from the side in the same plane. Interestingly, the only marine organism currently known to use

polarization signaling, the marine stomatopod (e.g., *Odontodactylus cultrifer* [39]), occupies relatively shallow benthic environments and uses dichroic signals in the red channel. Given the polarization characteristics of shallow marine benthos explored in this study, the stomatopod's red polarization signals may be highly useful under short distances for conspecific communication but are likely to degrade over longer distances. Hence polarized red light could constitute a more private communication channel than dichroic blue or green.

7. Conclusions

This study on various benthic surfaces shows that the Lambertian approximation with an appropriate reflectance spectrum facilitates accurate simulations in the full water column. Closure is attained between measurements and only those RT simulations, which incorporate a reflecting seafloor. Such a surface diminishes the DoLP from what it would be in optically deep water, where the seafloor is effectively invisible. The Lambertian surfaces used throughout this study

would not exist in reality, but they are designed to exhibit realistic benthic reflectances that increase upwelling radiance, to which the DoLP is inversely proportional. In red light, which is strongly attenuated by water molecules, the DoLP attains its maximum, whereas green and blue benthic signals are almost entirely transmitted through the water column and exert the seafloor's depolarizing effect. Variations in the IOPs can disrupt this pattern. Shifts in the scattering matrix can cause the DoLP to peak at scattering angles beyond the 90° at which it would in pure water. And CDOM as well as minerals and detritus, typically abundant in coastal waters, can strongly absorb blue light, mitigating the depolarizing effect of the seafloor in that spectral band.

Organisms with depolarizing camouflage could therefore adapt to hide in any benthic environment—be it sea grass, sand, or coral. Hiding above the benthos, in the shallow water column, is much more difficult, however. Red polarization signals may be highly useful under short distances for communication since polarization is well preserved in the red channel.

The AoLP is almost spectrally constant and independent of the bottom; therefore, it can be used for orientation outside of the principal scattering plane both in deep and shallow waters.

This work was supported by a Department of Defense (DOD) Office of Naval Research (ONR) Multi-University Research Initiative (MURI) grant N000140911054. The CCNY group also acknowledges partial support from the National Oceanic and Atmospheric Administration (NOAA) grant NA11SEC4810004, ONR grant N000141010368, and NASA grant NNX13AF44G. TAMU group acknowledges partial support from NSF grant OCE 1130906 and N000141110154 from ONR. The UCONN COLORS group acknowledges partial support from NASA grant NNX 13AH88G. We are grateful to the staff of the Keys Marine Laboratory, Layton, Florida, who provided outstanding support during our field campaign. We are also grateful to two anonymous reviewers for their helpful suggestions, which improved the quality of the paper.

References

1. A. Ivanoff and T. H. Waterman, "Elliptical polarisation of submarine illumination," *J. Mar. Res.* **16**, 255–282 (1958).
2. V. Timofeeva, "On study of polarization characteristics of light field in turbid media," *Dokl Akad Nauk SSSR* **140**, 361–363 (1961).
3. T. H. Waterman, "Polarization patterns in submarine illumination," *Science* **120**, 927–932 (1954).
4. A. Ivanoff and T. H. Waterman, "Factors, mainly depth and wavelength, affecting the degree of underwater light polarization," *J. Mar. Res.* **16**, 283–307 (1958).
5. R. Schwind, "Daphnia pulex swims towards the most strongly polarized light—a response that leads to 'shore flight'," *J. Exper. Bio.* **202**, 3631–3635 (1999).
6. T. W. Cronin and N. Shashar, "The linearly polarized light field in clear, tropical marine waters: spatial and temporal variation of light intensity, degree of polarization and e-vector angle," *J. Exp. Biol.* **204**, 2461–2467 (2001).
7. N. Shashar, S. Sabbah, and T. W. Cronin, "Transmission of linearly polarized light in seawater: implications for polarization signaling," *J. Exp. Biol.* **207**, 3619–3628 (2004).
8. H. M. Dierssen, R. C. Zimmerman, R. A. Leathers, T. V. Downes, and C. O. Davis, "Ocean color remote sensing of sea grass and bathymetry in the Bahamas Banks by high-resolution airborne imagery," *Limnol. Oceanogr.* **48**, 444–455 (2003).
9. C. D. Mobley, H. Zhang, and K. J. Voss, "Effects of optically shallow bottoms on upwelling radiances: bidirectional reflectance distribution function effects," *Limnol. Oceanogr.* **48**, 337–345 (2003).
10. R. C. Zimmerman, "A bio-optical model of irradiance distribution and photosynthesis in sea grass canopies," *Limnol. Oceanogr.* **48**, 568–585 (2003).
11. K. J. Voss, C. D. Mobley, L. K. Sundman, J. E. Ivey, and C. H. Mazel, "The spectral upwelling radiance distribution in optically shallow waters," *Limnol. Oceanogr.* **48**, 364–373 (2003).
12. H. Zhang and K. J. Voss, "Bidirectional reflectance and polarization measurements on packed surfaces of benthic sediments and spherical particles," *Opt. Express* **17**, 5217–5231 (2009).
13. M. McPherson, V. J. Hill, R. C. Zimmerman, and H. M. Dierssen, "The optical properties of Greater Florida Bay: implications for sea grass abundance," *Estuaries Coasts* **34**, 1150–1160 (2011).
14. C. Buonassissi and H. M. Dierssen, "A regional comparison of particle size distributions and the power-law approximation in oceanic and estuarine surface waters," *J. Geophys. Res.* **115**, C10028 (2010).
15. C. H. Mazel, "Diver-operated instrument for in situ measurement of spectral fluorescence and reflectance of benthic marine organisms and substrates," *Opt. Eng.* **36**, 2612–2617 (1997).
16. A. Morel, "Optical properties of pure water and pure sea water," in *Optical Aspects of Oceanography*, N. G. Jerlov and E. S. Nielsen, eds. (Academic, 1974), pp. 1–24.
17. J. E. Hansen and L. D. Travis, "Light scattering in planetary atmospheres," *Space Sci. Rev.* **16**, 527–610 (1974).
18. H. C. Van de Hulst, *Light Scattering by Small Particles* (Dover Publications, 1981).
19. Y. You, A. Tonizzo, A. A. Gilerson, M. E. Cummings, P. Brady, J. M. Sullivan, M. S. Twardowski, H. M. Dierssen, S. A. Ahmed, and G. W. Kattawar, "Measurements and simulations of polarization states of underwater light in clear oceanic waters," *Appl. Opt.* **50**, 4873–4893 (2011).
20. J. M. Sullivan and M. S. Twardowski, "Angular shape of the oceanic particulate volume scattering function in the backward direction," *Appl. Opt.* **48**, 6811–6819 (2009).
21. M. Twardowski, X. Zhang, S. Vagle, J. Sullivan, S. Freeman, H. Czerski, Y. You, L. Bi, and G. Kattawar, "The optical volume scattering function in a surf zone inverted to derive sediment and bubble particle subpopulations," *J. Geophys. Res.* **117**, C00H17 (2012).
22. A. Tonizzo, J. Zhou, A. Gilerson, M. S. Twardowski, D. J. Gray, R. A. Arnone, B. M. Gross, F. Moshary, and S. A. Ahmed, "Polarized light in coastal waters: hyperspectral and multiangular analysis," *Opt. Express* **17**, 5666–5682 (2009).
23. A. Tonizzo, A. Gilerson, T. Harmel, A. Ibrahim, J. Chowdhary, B. Gross, F. Moshary, and S. Ahmed, "Estimating particle composition and size distribution from polarized water-leaving radiance," *Appl. Opt.* **50**, 5047–5058 (2011).
24. E. P. Zege, L. L. Katsev, and I. N. Polonsky, "Multicomponent approach to light propagation in clouds and mists," *Appl. Opt.* **32**, 2803–2812 (1993).
25. H. H. Tynes, G. W. Kattawar, E. P. Zege, I. L. Katsev, A. S. Prikhach, and L. I. Chaikovskaya, "Monte Carlo and multi-component approximation methods for vector radiative transfer by use of effective Mueller matrix calculations," *Appl. Opt.* **40**, 400–412 (2001).
26. R. M. Pope and E. S. Fry, "Absorption spectrum (380–700 nm) of pure water. 2. Integrating cavity measurements," *Appl. Opt.* **36**, 8710–8723 (1997).

27. G. W. Kattawar, G. N. Plass, and S. J. Hitzfelder, "Multiple scattered radiation emerging from Rayleigh and continental haze layers. 1. Radiance, polarization, and neutral points," *Appl. Opt.* **15**, 632–647 (1976).
28. G. Zibordi, F. Mélin, S. B. Hooker, D. D'Alimonte, and B. Holben, "An autonomous above-water system for the validation of ocean color radiance data," *IEEE Trans. Geosci. Remote Sens.* **42**, 401–415 (2004).
29. S. Chandrasekhar, *Radiative Transfer* (Dover Books on Physics, 1960).
30. J. T. Adams, E. Aas, N. K. Hojerslev, and B. Lundgren, "Comparison of radiance and polarization values observed in the Mediterranean Sea and simulated in a Monte Carlo model," *Appl. Opt.* **41**, 2724–2733 (2002).
31. C. D. Mobley and L. K. Sundman, "Effects of optically shallow bottoms on upwelling radiances: inhomogeneous and sloping bottoms," *Limnol. Oceanogr.* **48**, 329–336 (2003).
32. J. Hedley and S. Enriquez, "Optical properties of canopies of the tropical sea grass *Thalassia testudinum* estimated by a three-dimensional radiative transfer model," *Limnol. Oceanogr.* **55**, 1537–1550 (2010).
33. M. P. Lesser and C. D. Mobley, "Bathymetry, water optical properties, and benthic classification of coral reefs using hyperspectral remote sensing imagery," *Coral Reefs* **26**, 819–829 (2007).
34. C. D. Mobley, "HydroLight users' guide".
35. H. M. Dierssen, R. C. Zimmerman, D. Burdige, and L. Drake, "Benthic ecology from space: optics and net primary production in sea grass and benthic algae across the Great Bahama Bank," *Mar. Ecol. Prog. Ser.* **411**, 1–15 (2010).
36. E. J. Hochberg and M. J. Atkinson, "Spectral discrimination of coral reef benthic communities," *Coral Reefs* **19**, 164–171 (2000).
37. A. Ibrahim, A. Gilerson, T. Harmel, A. Tonizzo, J. Chowdhary, and S. Ahmed, "The relationship between upwelling under-water polarization and attenuation/absorption ratio," *Opt. Express* **20**, 25662–25680 (2012).
38. P. C. Brady, K. A. Travis, T. Maginnis, and M. E. Cummings, "Polaro-cryptic mirror of the lookdown as a biological model for open ocean camouflage," *Proc. Natl. Acad. Sci. USA* **110**, 9764–9769 (2013).
39. T.-H. Chiou, S. Kleinlogel, T. Cronin, R. Caldwell, B. Loeffler, A. Siddiqi, A. Goldizen, and J. Marshall, "Circular polarization vision in a stomatopod crustacean," *Current Biology* **18**, 429–434 (2008).